Photoacoustics 33 (2023) 100548

Contents lists available at ScienceDirect

Photoacoustics

journal homepage: www.elsevier.com/locate/pacs

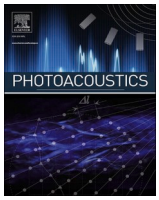

Broadband transparent ultrasound transducer with polymethyl methacrylate as matching layer for *in vivo* photoacoustic microscopy

Jiaming Zhang [a,1], Xing Long [b,1], Guangjie Zhang [b], Zhongtian Ma [b], Wenzhao Li [b], Yibing Wang [b], Fan Yang [a], Riqiang Lin [a], Changhui Li [b,c,*], Kwok-Ho Lam [a,d,**]

[a] Department of Electrical Engineering, The Hong Kong Polytechnic University, Hong Kong, China
[b] Department of Biomedical Engineering, College of Future Technology, Peking University, Beijing 100871, China
[c] National Biomedical Imaging Center, Peking University, Beijing 100871, China
[d] Centre for Medical and Industrial Ultrasonics, James Watt School of Engineering, University of Glasgow, Glasgow, Scotland, UK

ARTICLE INFO

Keywords:
Transparent ultrasound transducer
Broadband transducer
Photoacoustic imaging
Optical-resolution photoacoustic microscopy

ABSTRACT

Photoacoustic imaging (PAI) uniquely combines optics and ultrasound, presenting a promising role in biomedical imaging as a non-invasive and label-free imaging technology. As the traditional opaque ultrasound (US) transducers could hinder the transportation of the excitation light and limit the performance of PAI system, piezoelectric transparent ultrasonic transducers (TUTs) with indium tin oxide (ITO) electrodes have been developed to allow light transmission through the transducer and illuminate the sample directly. Nevertheless, without having transparent matching materials with appropriate properties, the bandwidth of those TUTs was generally narrow. In this work, we propose to employ polymethyl methacrylate (PMMA) as the matching layer material to improve the bandwidth of lithium niobate (LN)-based TUTs. The effects of PMMA matching layer on the performance of TUTs have been systematically studied. With the optimized PMMA matching layer, the very wide bandwidth of $>$ 50 % could be achieved for the TUTs even with different transducer frequencies, leading to the great enhancement of axial resolution when compared to the similar reported work. In addition, the imaging performance of the developed TUT prototype has been evaluated in a PAI system and demonstrated by both phantom and *in vivo* small animal imaging.

1. Introduction

Photoacoustic imaging (PAI), which combines high optical contrast and high penetration of ultrasound (US), is a powerful and advanced non-invasive functional imaging technology. PAI has now been widely used in the field of evaluation of lesions [1,2], brain imaging [3,4], and early cancer detection and diagnosis [5,6]. However, conventional US transducers are opaque. The PAI system either employs the light illumination from sides of the transducer or uses complex optical design to co-align laser and acoustic beams, leading to bulky and inefficient system designs. To partially resolve the issue, a ring shaped or hollow US transducer was proposed to allow the laser beam to pass through [7–10], but the central orifice in the transducer may lead to the adverse effect on electrical properties and acoustic energy [11], resulting in the degradation of image quality [12]. In recent years, although the pure-optical ultrasound detection method has gained much progress [13–15], it is still challenging to make those non-piezoelectric transparent pure optical sensors into a parallel array, which substantially limits the implementation.

The alternative solution is to develop transparent piezoelectric transducers to allow the laser beam to pass through it and illuminate the sample directly. Due to the transparent nature and high electromechanical coupling capability, lithium niobate (LN) was firstly employed to develop a piezoelectric-based transparent US transducer (TUT) with sputtered transparent indium tin oxide (ITO) electrodes as a substitution of chrome/gold electrodes [16–18]. Nevertheless, the high sheet resistance of ITO and the single matching layer scheme limit both sensitivity and bandwidth of TUTs. Several methods have been developed to improve the sensitivity of TUTs, including making use of large aperture size to achieve appropriate electrical impedance matching [19],

* Corresponding author at: Department of Biomedical Engineering, College of Future Technology, Peking University, Beijing 100871, China.
** Corresponding author at: Department of Electrical Engineering, The Hong Kong Polytechnic University, Hong Kong, China.
E-mail addresses: chli@pku.edu.cn (C. Li), kwokho.lam@glasgow.ac.uk (K.-H. Lam).
[1] These authors contribute equally.

https://doi.org/10.1016/j.pacs.2023.100548
Received 1 June 2023; Received in revised form 20 July 2023; Accepted 22 August 2023
Available online 23 August 2023

Table 1
Properties of active and passive materials.

	Sound velocity (m/s)	Density (kg/m^3)	Acoustic impedance (MRayl)
LN	7340	3300	34.0
Epotek-301	2650	1132	3.0
PMMA	2750	1175	3.2

implementing lens-focused design [20,21], using silver nanowires as electrode [22], and employing novel transparent AC-poled lead magnesium niobate-lead titanate (PMN-PT) single crystals as an active layer [23]. However, those TUTs still exhibited narrow bandwidth. Besides, both LN and AC-poled PMN-PT materials own high acoustic impedance (>30 MRayl), which is difficult to achieve acoustic matching to biological tissue (~1.5 MRayl) due to the limited choices of transparent material as matching layers. Although the ITO-coated polyvinylidene difluoride (PVDF) with much lower acoustic impedance is one of the potential candidates especially with high receiving sensitivity [24], the very low clamped dielectric constant led to the large aperture size for electrical impedance matching, which is not suitable for compact photoacoustic microscopy (PAM) applications [25]. On the other hand, the relatively small aperture size of PVDF would lead to the degradation of transducer performance [26,27]. Consequently, efforts have been made to develop transparent matching layers for LN-based TUTs. The conventional approach of casting matching layers, which generally consists of metal powders and epoxy, is challenging to achieve transparency and maintain appropriate acoustic impedances simultaneously due to inherent heterogeneity of materials. A novel transparent matching layer design, consisting of glass beads and epoxy, has been proposed with tunable acoustic impedance. However, the glass beads would scatter the light, which is not desired in the high-resolution PAM application [28]. Another design was with a quarter-wavelength ($\lambda/4$)-thick glass and Parylene C as two matching layers, but the TUT turned into a dual-frequency mode with a narrow bandwidth at its original resonant frequency and dispersed energy at resonances [22]. Although the performance of TUTs could be optimized by tuning the thicknesses of two matching layers, the approach may not be universal especially when the transducer frequency is out of the initial designated value [29]. Besides, in some cases of the TUT design, the measured center frequency was quite different from the simulation result [30]. Thus, the development of broadband TUTs based on the reported acoustic matching methods is still challenging especially for PAI applications using the high-frequency TUTs (>20 MHz) [31].

Although the transparent Parylene C has widely been used as matching and protective layers of LN-based TUTs, its acoustic impedance (2.7 MRayl) is still far from the theoretical value for adopting the single matching layer scheme (4.25 MRayl) [32]. As a common transparent polymer material, polymethyl methacrylate (PMMA) owns relatively high acoustic impedance (3.2 MRayl) and low density [33,34], which is close to the desired value of the LN-based TUT with a single matching layer and may alleviate a mass-load effect. Therefore, we investigate PMMA as the matching layer for the TUT in this study. As a thick layer attached on the transducer surface may lead to the dual-frequency phenomenon [35,36], the study on the thickness of PMMA is very critical. In addition, PAI of both phantom and *in vivo* animal model were conducted to evaluate the performance of LN-based TUT with the PMMA matching layer.

2. Methods and materials

2.1. Transducer design and fabrication

A double-side polished 36° rotated Y-cut LN was purchased from Shanghai Institute of Optics and Fine Mechanics. Transparent epoxy (Epotek 301, Epoxy Technology Inc., USA) was used as a backing layer as well as a bonding agent. The acoustic properties of transparent PMMA layer were measured, including longitudinal sound velocity, density, and acoustic impedance. All material parameters are listed in Table 1.

ITO was DC sputtered from an ITO target (In_2O_3/SnO_2 90/10 wt%, Kurt J. Lesker Company, USA) on one side of LN at a power of 45 W and an Argon flow of 30 sccm for 80 min (Explorer 14, Denton Vacuum, USA). The LN wafer was then cut into the desired square shape and attached on a glass slide with the electrode side up. After placed the LN wafer in a 10 mm-diameter brass housing, a co-axial cable was connected to the bottom electrode and brass housing using the conductive silver epoxy (E-Solder 3022, Von Roll Isola Inc., USA). After cured at 60 °C for 3 h, the degassed transparent epoxy backing layer was filled into the brass housing. The transducer was removed from the glass slide after cured at 65 °C for 2 h. The aforementioned sputtering process was conducted to deposit the ITO electrode on the transducer surface to achieve ground connection. The PMMA layer was lapped and polished to the desired thickness, and then bonded to the transducer surface using the degassed transparent epoxy. External pressure was applied to make the bonding layer as thin as possible. Fig. 1(a) and (b) show the photograph and the cross-sectional schematic view of the developed TUT.

A 20-MHz TUT was fabricated along with the conventional US transducer technology [37] using a 150 μm-thick LN with an aperture size of 9 mm × 9 mm. To study the acoustic matching effect on the TUT performance, the PMMA layers with different thicknesses, including 34 μm (= $\lambda/4$), 24 μm and 17 μm, were attached as the matching layer of TUT. The optimized matching layer design was also applied on a 30-MHz TUT to further verify the validity of the proposed scheme.

2.2. Transducer characterizations

To measure the pulse-echo response, the fabricated TUT was mounted on a holder and immersed in distilled water. The TUT was excited by a pulser-receiver (DPR500, JSR Ultrasonics, USA) with an energy of 12.4 μJ and a pulse repetition frequency of 200 Hz. Echo signal was acquired by a data acquisition (DAQ) card, and analyzed by fast Fourier transform (FFT) to determine the center frequency (f_c) and − 6 dB bandwidth (BW) as:

$$f_c = \frac{f_1 + f_2}{2} \quad (1)$$

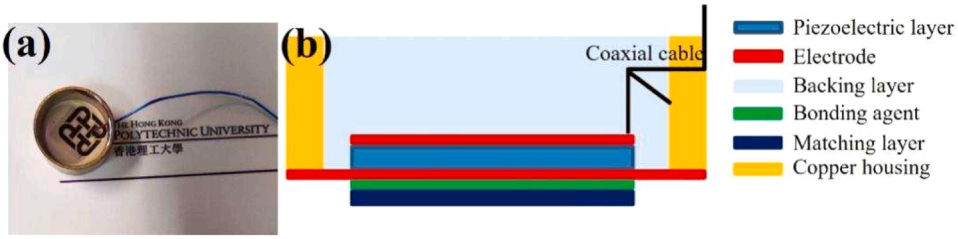

Fig. 1. (a) Photograph and (b) cross-sectional schematic view of the prototype of TUT.

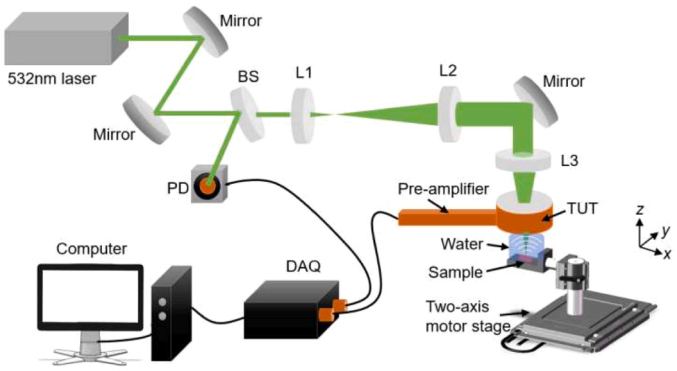

Fig. 2. Schematic of optical-resolution photoacoustic microscopy (OR-PAM) system based on the developed TUTs. BS: beam sampler; PD: photodiode; L1, L2, and L3: plane convex lenses with focal lengths of 25.4, 150, and 30 mm, respectively.

$$BW = \frac{f_2 - f_1}{f_c} \tag{2}$$

where f_1 and f_2 are lower and upper − 6 dB frequencies, respectively. The TUT was then connected to an impedance analyzer (Agilent 4294 A, Agilent Technologies, USA) for electrical impedance analysis, where the resonant frequency (f_r) and anti-resonant frequency (f_a) were obtained. The effective electromechanical coupling coefficient (k_{eff}) was calculated as:

$$k_{eff} = \sqrt{1 - \frac{f_r^2}{f_a^2}} \tag{3}$$

Two-way insertion loss (*IL*) was measured using a function generator that was used to generate a burst of 10-cycle sine wave with a specific peak-to-peak amplitude (V_0). The peak-to-peak amplitude of the echo signal (V_1) was acquired using a digital oscilloscope with 1 MΩ coupling. *IL* was calculated as

$$IL = 20\log\frac{V_1}{V_0} \tag{4}$$

The optical transmission efficiency of TUT was measured by a spectrometer (USB4000, Ocean optics Inc.). The transmission efficiency was obtained by calculating the ratio of light intensity before and after passing through the TUT.

2.3. PAI system

To demonstrate the PAI application of the 20-MHz TUT with the optimized PMMA matching layer, a refection-mode PAM system was customized for evaluating the performance of TUT *via* imaging both phantoms and *in vivo* rodents.

The PAM system is shown in Fig. 2, which employed a pulsed laser (AO-S-532, Changchun New Industries Optoelectronics Technology Co., Ltd.; 532 nm wavelength; 4 ns pulse duration) to excite PA signal. A beam sampler (glass slide) was used to reflect small part of the laser beam to a photodiode (DET10A/M, Thorlabs Inc.) to synchronize the signal acquisition. The laser beam passed through a beam expander system consisting of two convex lenses before focusing by a convex lens with a focal length of 30 mm. The focused beam passed through the TUT and then emitted onto the target sample. The two-axis motor stage (MS-2000, Applied Scientific Instrumentation) was used to scan the sample along the *x*-y plane. The acquired PA signal was amplified by a home-made low-noise pre-amplifier (Gain: 40 dB, Bandwidth: 35 MHz, Noise level: 5nV/$\sqrt{\text{Hz}}$), which was directly connected to the TUT without using any external cable and recorded by a DAQ card with a sampling rate of 200 MHz (CompuScope 14200, Gage, Canada, 14 bit). The gap between the TUT and imaging sample was filled by a drop of distilled water as an ultrasound coupling medium.

3. Results and discussion

3.1. Simulation study

PiezoCAD software (Sonic Concepts, WA, USA) based on Krimholtz, Leedom and Matthaei (KLM) model was employed to simulate the transducer performance. The LN-based TUTs with the thickness of 150 μm and the aperture size of 9 mm × 9 mm were modeled to simulate the pulse-echo performance in terms of matching layer configuration. Fig. 3(a)–(c) show the simulated pulse-echo response of TUTs without matching layer, with λ/4-thick Parylene, and λ/4-thick PMMA as matching layers, respectively. Compared with the TUT with the Parylene matching layer, the one with the PMMA matching layer exhibited the wider bandwidth as well as the higher sensitivity. The simulated results indicated that PMMA as the matching layer could improve the performance of TUT much effectively when compared to Parylene.

3.2. Acoustic response of TUTs

Fig. 4(a) shows the experimental results of pulse-echo response of a TUT with the aperture size of 9 mm × 9 mm and without matching layer, showing a *BW* of ~17 % and a peak-to-peak received voltage of 0.8 V. Fig. 4(b)–(d) show the measured pulse-echo responses of TUTs with the 34 μm, 24 μm and 17 μm-thick PMMA matching layers, respectively.

As shown in Fig. 4(b), the TUT with the theoretical λ/4-thick PMMA matching layer exhibited the most enhanced pulse-echo sensitivity among the TUTs when compared to other thicknesses of PMMA layer. Nevertheless, an additional peak appeared at ~13 MHz, indicating that

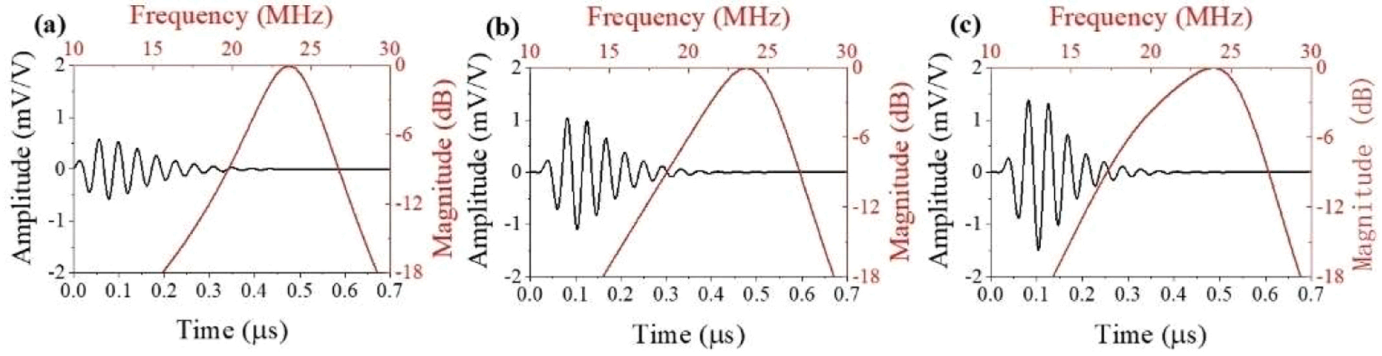

Fig. 3. Simulated pulse-echo responses of LN-based TUTs (a) without matching layer, (b) with λ/4-thickParylene matching layer, and (c) λ/4-thick PMMA matching layer.

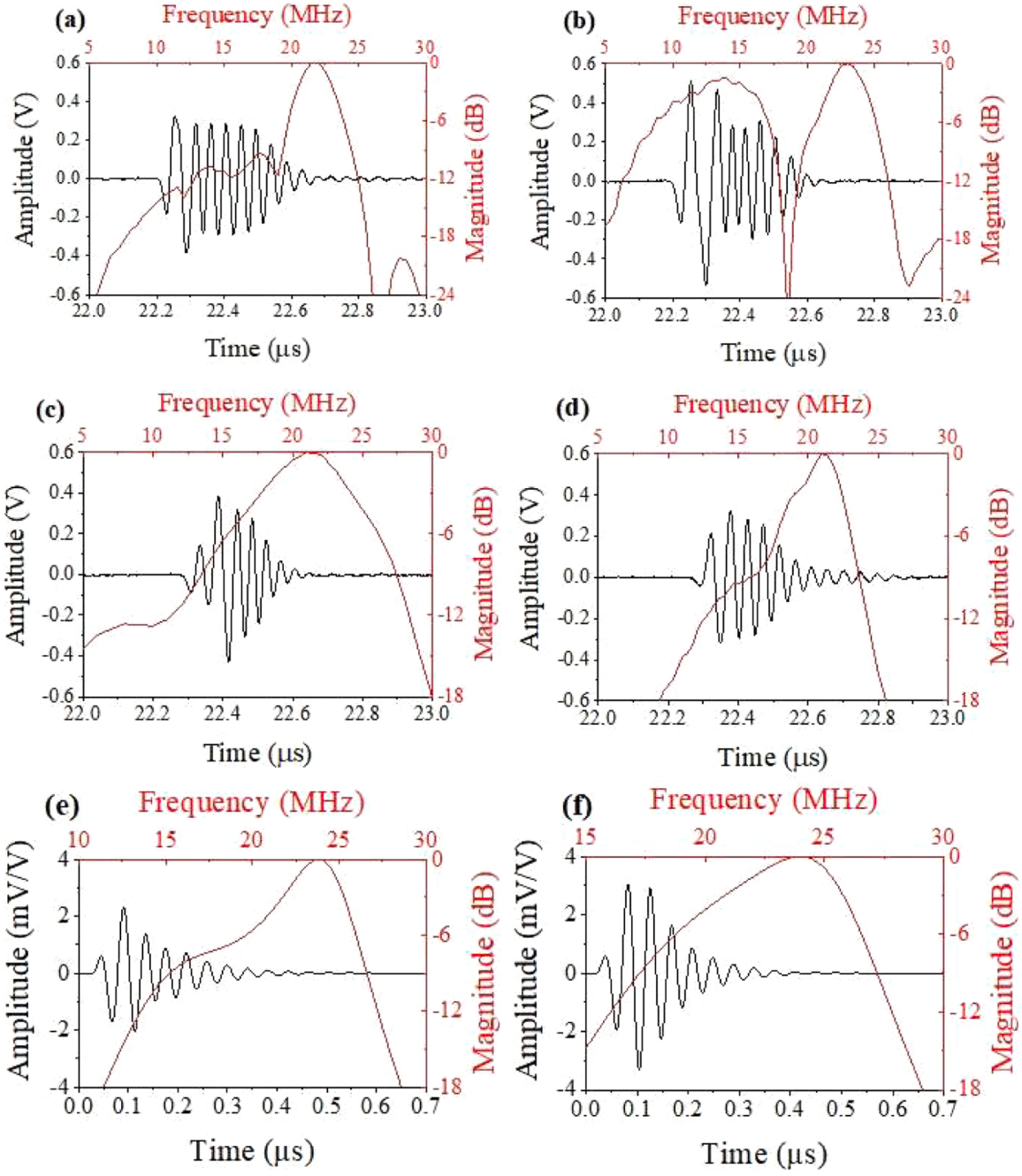

Fig. 4. Measured pulse-echo responses of 20-MHz TUTs(a) without matching layer and with the (b)34 μm (= $\lambda/4$), (c) 24 μm, and (d) 17 μm-thick PMMA matching layers, respectively. Simulated pulse-echo response of 20-MHz TUT with (e) 34 μm (= $\lambda/4$) and (f) 24 μm-thick PMMA matching layers.

the TUT with the $\lambda/4$-thick matching layer was a dual-frequency transducer. The phenomenon may be induced by the mass-load effect of a bonding layer, which was also reported in literature [22,23]. Although the *BW* at the lower frequency reached 71.4 %, the *BW* at the designed center frequency was still limited as 19.2 %. For the TUT with the 24 μm-thick PMMA matching layer (Fig. 4(c)), the *BW* was significantly widened to 50.4 % with the center frequency of 20.9 MHz, while the sensitivity of TUT was almost the same as that of TUT without matching layer. Taking into account of similar acoustic impedances of PMMA and degassed transparent epoxy, both matching and bonding layers are likely to contribute together to form a $\lambda/4$ matching layer. Further reduction of the PMMA thickness (17 μm) led to the lower sensitivity (Fig. 4(d)) when compared to the TUT with the 24 μm-thick PMMA layer, though the *BW* was still better than that of the TUT without matching layer. Consequently, the difference in the thickness between the $\lambda/4$-thick matching layer and the optimized PMMA matching layer was considered as the thickness of bonding layer. Fig. 4(e) and (f) show

Table 2
Acoustic performance of TUTs with different thicknesses of PMMA matching layer.

Aperture size (mm × mm)	PMMA thickness (μm)	f_c (MHz)	*BW* (%)	Echo amplitude (V)
9.0 × 9.0	34	12.75/ 22.9	71.4/ 19.2	1.04
9.0 × 9.0	24	20.8	50.2	0.80
9.0 × 9.0	17	20.4	27.2	0.64
6.3 × 6.3	13	27.8	56.1	0.55

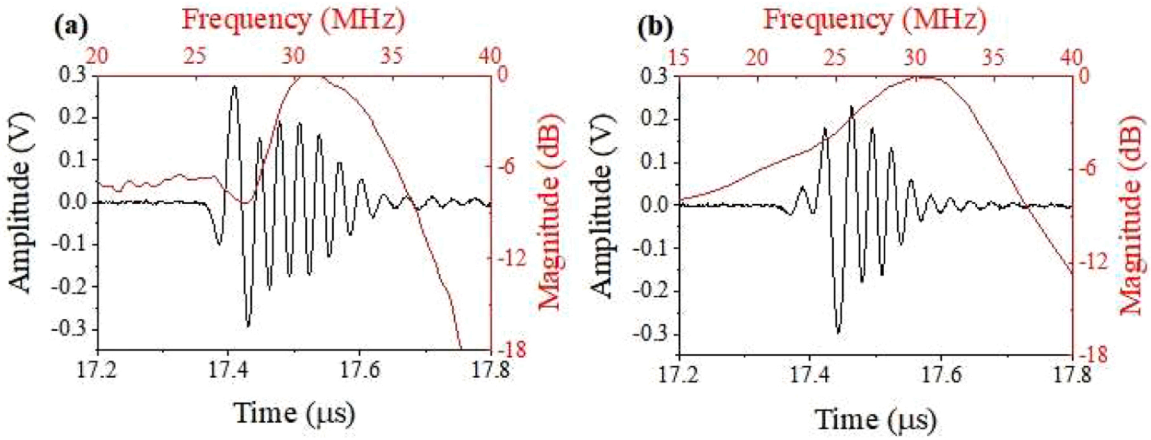

Fig. 5. (a) Measured pulse-echo responses of 30-MHz TUTs without matching layer and (b) with the 13 μm-thick PMMA matching layer.

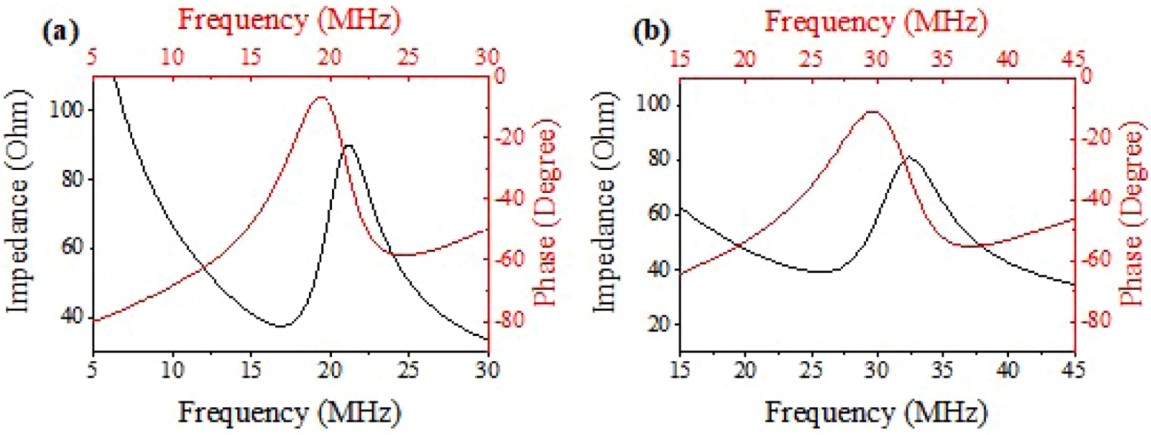

Fig. 6. Measured impedance/phase spectra of (a)a 20-MHz TUT with the 24 μm-thick PMMA matching layer, and (b) a 30-MHz TUT with the 13 μm-thick PMMA matching layer.

the simulated pulse-echo responses of TUTs with 34 μm and 24 μm-thick PMMA matching layers, respectively, in which the bonding layer was set as 10 μm. The simulation results indicate that the TUT with the 24 μm-thick PMMA layer exhibited the optimized performance on both bandwidth and sensitivity. Similar to Fig. 4(b), an additional peak was shown at 15 MHz in the simulated FFT waveform of TUT with the 34 μm-thick PMMA layer, leading to the lower sensitivity due to the energy allocation to vibrations at two different frequencies. Table 2 summarizes the measured results.

To explore the potential of PMMA matching on the development of TUTs, the study was further performed on the TUTs with higher frequency. Based on the investigations of the 20-MHz TUTs, the difference in the thickness between the $\lambda/4$-thick matching layer and the optimized PMMA matching layer was considered as the thickness of bonding layer. Thus, a 13 μm-thick PMMA matching layer was applied on a 30-MHz LN-based TUT. Fig. 5(a) and (b) show the measured pulse-echo responses of 30-MHz TUTs without and with the PMMA matching layer, respectively. After attached with the 13 μm-thick PMMA layer, the *BW* of TUT significantly increased from 21.4 % to 56.1 %, while the center frequency slightly decreased from 31.8 MHz to 27.8 MHz. The *BW* was very wide, which is ~65 % increment even when compared to the maximum *BW* of high-frequency TUTs with a single matching layer reported in literature[18]. The results show that the proposed scheme was still valid even for developing the TUTs with higher center frequency.

The *IL* of the 20-MHz TUT with a 24 μm-thick PMMA matching layer was measured as 28.4 dB. The acoustic receiving sensitivity was also measured, in which a calibrated commercial 20-MHz US transducer (V317-SM, Olympus NDT Inc.) was driven by a pulser-receiver (5072PR, Olympus) to generate the acoustic wave while the signal was detected by the TUT. The signal-to-noise (SNR) was ~30 dB without averaging, and the noise equivalent pressure (NEP) was calculated to be ~66 Pa at 20 MHz.

3.3. Electrical properties

Fig. 6(a) and (b) show the electrical impedance/phase spectra of the 20-MHz TUT with the 24 μm-thick PMMA matching layer and those of the 30-MHz TUT with the 13 μm-thick PMMA matching layer, respectively. All transducers exhibited a pure and strong resonance without any spurious mode, and their electrical impedances closed to the optimized value (~50 Ω) at the corresponding center frequencies. Besides, their k_{eff} were reasonably high, which were calculated as 0.60 and 0.59, respectively.

3.4. Optical property and PAI performance

The broadband 20-MHz TUT with 24 μm-thick PMMA matching layer was employed to conduct optical measurement due to its large aperture size. Fig. 7(a) shows the measured optical transmission efficiency of TUT with the PMMA matching layer to be larger than 70 % in the wavelength range of 500 – 900 nm. Although the optical transmission efficiency at 532 nm reduced to ~75 % due to the attached PMMA layer, the laser beam could reach the target with enough energy for imaging [30]. Moreover, the peak transmittance could reach close to

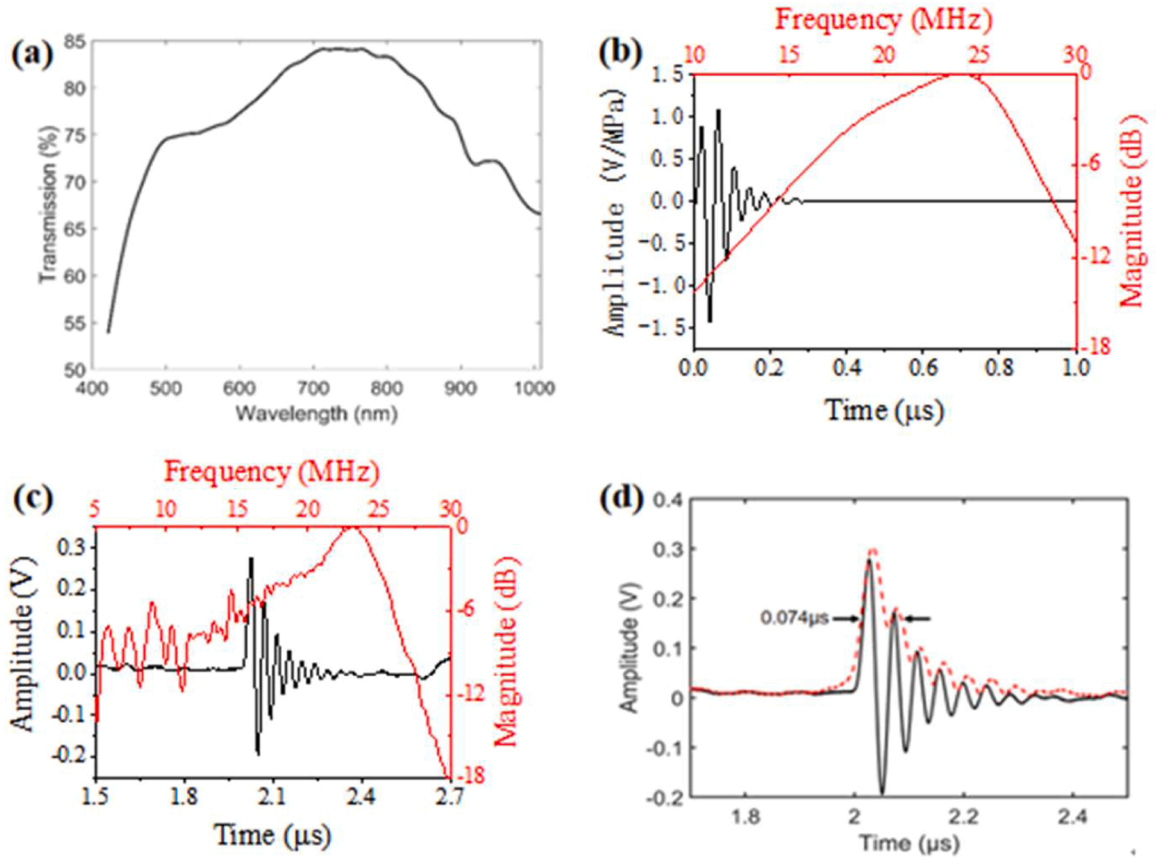

Fig. 7. (a) Measured optical transmission efficiency of the TUT. (b) Simulated one-way receive response of the TUT. (c) Time-domain response of TUT to PA signal and corresponding frequency-domain response of a 20-MHz TUT with 24 μm-thick PMMA matching layer. (d) Axial resolution of an OR-PAM system with TUT, where the black line is the time-domain signal and the red dashed line is the Hilbert enveloped curve.

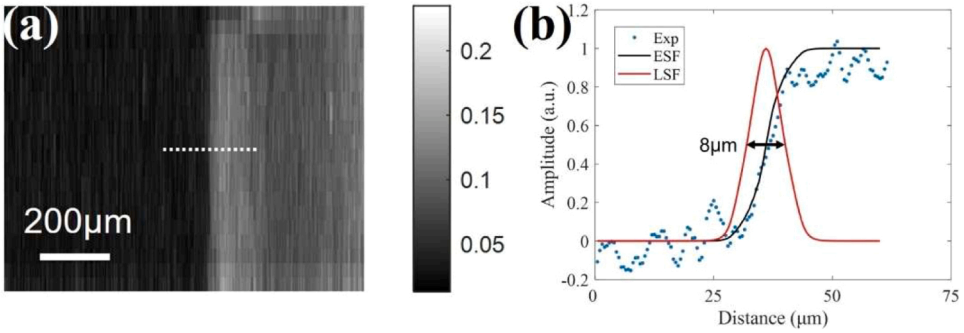

Fig. 8. (a) PA MAP image of a sharp razor blade. (b) Lateral resolution of an OR-PAM system with TUT, where blue dots are the experimental data, a black line is the fitted ESF, and a red line is the derived LSF.

85 % between 700 nm and 800 nm, which is optimal for deep tissue PAI applications.

To test the PA signal response and bandwidth of the TUT system, a short pulse laser was employed to excite a thin layer of oil marker painted onto a thick glass block to generate a broadband PA signal. Fig. 7 (c) shows the detected time-domain PA signal without average and the corresponding frequency spectrum after normalized at the peak value at 20 MHz, showing a center frequency of 20.8 MHz and a *BW* of 49.3 %, which matched well with the simulated one-way receive response of the TUT (Fig. 7(b)). The theoretical value of axial resolution was calculated from 0.88 *v/BW*, which depends on the bandwidth of the TUT (*BW*) and the acoustic speed (*v*)[38]. Although the reported work also achieved the similar PA bandwidth with the TUT employing a transparent matching layer consisting of epoxy and glass beads (40 % volume fraction), the TUT with the PMMA layer owns higher optical transmission efficiency without light scattering. As OR-PAM requires tight light focusing, the TUT with the PMMA layer is more suitable for this application. Fig. 7(d) shows the absolute value after performed the Hilbert transform on the time-domain response of TUT to the PA signal. The axial resolution of the system was 111 μm obtained from the full-width half-maximum (FWHW) of the envelope curve, which is close to the theoretical value (126 μm). The broadband TUT led to the improved axial resolution when compared to the reported TUT-based work even operated at higher center frequency [21].

The imaging capability of the 20-MHz TUT with the 24 μm-thick PMMA matching layer was evaluated using the OR-PAM system as

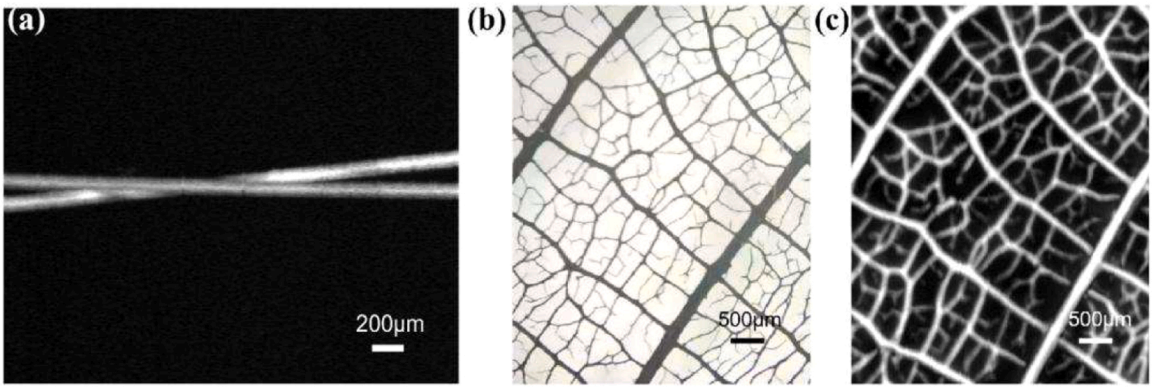

Fig. 9. (a) PA imaging of a cross of human hairs. (b) Light field microscope photograph and (c) PA imaging of the ink-stained leaf skeleton phantom.

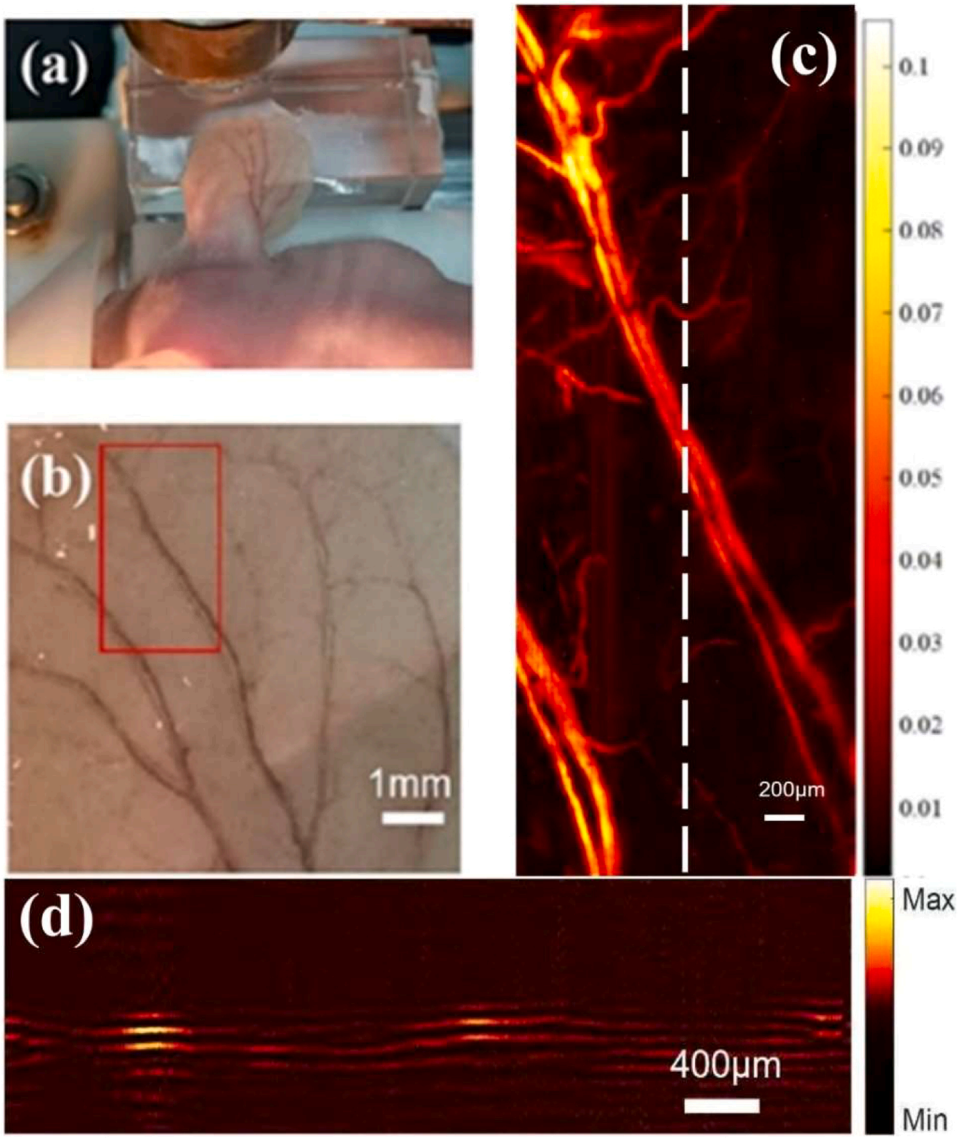

Fig. 10. Photographs of (a) the setup of mouse ear, and (b) *in vivo* imaging area. (c) MAP image of *in vivo* vascular networks in the area indicated by the box in (b). (d) Reconstructed depth-resolved slides at the location marked with a white dash line of (c).

shown in Fig. 2. The lateral resolution of system was measured by imaging the cutting edge of a razor blade at a scanning step size of 0.5 μm. The maximum amplitude projection (MAP) image of blade is shown in Fig. 8(a), which was averaged for 10 times. The edge spread function (ESF) is shown in Fig. 8(b), and the line spread function (LSF) is the first derivative of ESF. Then, the lateral resolution of the system was

calculated to be 8 μm based on the FWHW of the LSF.

The PAI performance of the 20-MHz TUT with the 24 μm-thick PMMA matching layer was evaluated *via* phantom and *in vivo* small animal models. A cross of hairs and leaf veins were employed as the phantom models. To image a cross of hairs, a step size of 2 μm in x direction and 5 μm in y direction was used to perform a 2 mm × 3 mm scanning area. The repetition rate of the 532-nm pulsed laser was 1 kHz and the sampling rate of the acquisition card was set to 200 MHz. The reconstructed MAP PA image without averaging is shown in Fig. 9(a). To image the ink-stained leaf skeleton phantom, a step size of 5 μm was adopted in both x and y directions. Even with a more complex structure, the OR-PAM imaging result of the leaf vein network corresponded well with the photograph taken by the light field microscope, as shown in Fig. 9(b) and (c). Both phantom studies showed high contrast and resolution of the system using the developed TUT.

A BALB/c nude mouse was used for the *in vivo* imaging experiment as shown in Fig. 10(a) and (b). The mouse was first anesthetized by inhaling isoflurane gas and then fixed on the translation stage. The distance between the mouse ear and TUT was ~1.2 mm, and a drop of distilled water was used as the ultrasound coupling medium. The PA signal was acquired by a step size of 1 μm in x direction and a step size of 5 μm in y direction with data averaging for 10 times. The scanning area was 1.5 mm × 4.2 mm. The laser energy on the surface of mouse ear skin was measured to be ~1 μJ, which slightly exceeded the maximum recommended value of ANSI for safe use of lasers [39]. An infrared lamp was used to maintain the body temperature of the mouse during the experiment. All research work performed in the laboratory followed the protocols that were approved by the Institutional Animal Care and the Use Committee of Peking University. The PA MAP image of mouse ear is shown in Fig. 10(c), in which both capillaries and the two large accompanying arteries and veins were clearly reconstructed. Fig. 10(d) shows one of the reconstructed depth-resolved slides at the location marked with a white dash line of Fig. 10(c). The locations of main vasculature are in good agreement of MAP images of vascular networks in the area. Some reflected signals were mainly caused by the light backing layer of TUT. Although the optimal thickness design of the matching layer improves the − 6 dB bandwidth and enhances the full-width half maximum (FWHM) resolution, the design introduces a prolonged ringing tail in the temporal echo response that can constrain the effective resolution of the imaging system. In situations where a weak blood vessel signal is positioned beneath a strong blood vessel signal in terms of depth, the weak signal may be overwhelmed by the long ringing tail of the strong blood signal. Consequently, this may lead to the inability to distinguish between the two blood vessels, thereby causing a reduction in the actual resolution. Besides exploring other matching materials, another potential future approach to mitigate this effect involves advanced signal processing such as deconvolution or machine learning.

4. Conclusion

The PMMA was successfully implemented as a matching layer on the development of TUTs. The optical transmittance was over 70 % in the wide range of wavelength. With the optimized thickness of PMMA matching layer, the bandwidth of TUTs was significantly improved to over 50 % while the designated center frequency was only slightly decreased. As the approach could also be applied to the TUT with other frequency, the universal scheme owned great potential for the development of high-frequency TUTs. Besides, we demonstrated very good performance of TUT in PAI, including phantom and *in vivo* small animal imaging. Although the sensitivity was not enhanced due to the acoustic attenuation of bonding agent, the PAM was successfully demonstrated with the developed TUT. It is worth noting that the proposed PMMA matching layer scheme offers a new path to enhance the performance of TUTs without the limitation of center frequency. Besides, the scheme could be used for developing transparent arrays to improve the imaging quality [40]. There are still some rooms to further improve the performance of the existing design. The light backing of TUT cannot absorb the backside waves effectively, causing signal reverberations and leading to the limited bandwidth. Future work may focus on the study of transparent backing layer material with high acoustic impedance and acoustic attenuation. Besides, as the receiving sensitivity of TUT with PMMA layer was relatively low, the laser energy employed was slightly high. One of the potential solutions is to optimize the ITO sputtering process to further enhance the optical transmission efficiency. Alternatively, a focused transducer design can also increase the receiving sensitivity.

Declaration of Competing Interest

The authors declare that they have no known competing financial interests or personal relationships that could have appeared to influence the work reported in this paper.

Data availability

The data that has been used is confidential.

Acknowledgements

The authors gratefully acknowledge support from the following grants: Hong Kong Research Impact Fund (R5029-19), Hong Kong General Research Fund (15220920), the National Key Research and Development Program from the Ministry of Science and Technology of the People's Republic of China (No. 2017YFE0104200), the National Natural Science Foundation of China (No. 81421004), and the National Key Instrumentation Development Project from the Ministry of Science and Technology of the People's Republic of China (No. 2013YQ030651).

References

[1] S. Iskander-Rizk, P. Kruizinga, R. Beurskens, G. Springeling, F. Mastik, N.M.S. de Groot, P. Knops, A.F.W. van der Steen, G. van Soest, Real-time photoacoustic assessment of radiofrequency ablation lesion formation in the left atrium, Photoacoustics 16 (2019), 100150, https://doi.org/10.1016/j.pacs.2019.100150.

[2] R. Cheng, J. Shao, X. Gao, C. Tao, J. Ge, X. Liu, Noninvasive assessment of early dental lesion using a dual-contrast photoacoustic tomography, Sci. Rep. 6 (1) (2016) 21798, https://doi.org/10.1038/srep21798.

[3] Y. Junjie, V.W. Lihong, Photoacoustic brain imaging: from microscopic to macroscopic scales, Neurophotonics 1 (1) (2014), 011003, https://doi.org/10.1117/1.NPh.1.1.011003.

[4] X. Zhu, Q. Huang, A. DiSpirito, T. Vu, Q. Rong, X. Peng, H. Sheng, X. Shen, Q. Zhou, L. Jiang, U. Hoffmann, J. Yao, Real-time whole-brain imaging of hemodynamics and oxygenation at micro-vessel resolution with ultrafast wide-field photoacoustic microscopy, Light Sci. Appl. 11 (1) (2022) 138, https://doi.org/10.1038/s41377-022-00836-2.

[5] G. Zhang, W. Li, M. Yang, C. Li, Developing a photoacoustic whole-breast imaging system based on the synthetic matrix array, Front. Phys. 8 (2020), https://doi.org/10.3389/fphy.2020.600589.

[6] L. Lin, L.V. Wang, The emerging role of photoacoustic imaging in clinical oncology, Nat. Rev. Clin. Oncol. 19 (6) (2022) 365–384, https://doi.org/10.1038/s41571-022-00615-3.

[7] P. Wang, T. Ma, M.N. Slipchenko, S. Liang, J. Hui, K.K. Shung, S. Roy, M. Sturek, Q. Zhou, Z. Chen, J.-X. Cheng, High-speed intravascular photoacoustic imaging of lipid-laden atherosclerotic plaque enabled by a 2-kHz barium nitrite Raman laser, Sci. Rep. 4 (1) (2014) 6889, https://doi.org/10.1038/srep06889.

[8] J. Xiao, Y. Li, W. Jin, K. Peng, Z. Zhu, B. Wang, Photoacoustic endoscopy with hollow structured lens-focused polyvinylidine fluoride transducer, Appl. Opt. 55 (9) (2016) 2301–2305, https://doi.org/10.1364/AO.55.002301.

[9] W. Liu, D.M. Shcherbakova, N. Kurupassery, Y. Li, Q. Zhou, V.V. Verkhusha, J. Yao, Quad-mode functional and molecular photoacoustic microscopy, Sci. Rep. 8 (1) (2018) 11123, https://doi.org/10.1038/s41598-018-29249-1.

[10] H. Kim, J.Y. Kim, S. Cho, J. Ahn, Y. Kim, H. Kim, C. Kim, Performance comparison of high-speed photoacoustic microscopy: opto-ultrasound combiner versus ring-shaped ultrasound transducer, Biomed. Eng. Lett. 12 (2) (2022) 147–153, https://doi.org/10.1007/s13534-022-00218-y.

[11] K.H. Lam, Y. Chen, K. Au, J. Chen, J.Y. Dai, H.S. Luo, Kerf profile and piezoresponse study of the laser micro-machined PMN-PT single crystal using 355nm Nd:YAG, Mater. Res. Bull. 48 (9) (2013) 3420–3423, https://doi.org/10.1016/j.materresbull.2013.05.025.

[12] J. Yao, L.V. Wang, Sensitivity of photoacoustic microscopy, Photoacoustics 2 (2) (2014) 87–101, https://doi.org/10.1016/j.pacs.2014.04.002.
[13] B. Dong, C. Sun, H.F. Zhang, Optical detection of ultrasound in photoacoustic imaging, IEEE Trans. Biomed. Eng. 64 (1) (2017) 4–15, https://doi.org/10.1109/TBME.2016.2605451.
[14] X. Zhu, Z. Huang, G. Wang, W. Li, D. Zou, C. Li, Ultrasonic detection based on polarization-dependent optical reflection, Opt. Lett. 42 (3) (2017) 439–441, https://doi.org/10.1364/OL.42.000439.
[15] G. Wissmeyer, M.A. Pleitez, A. Rosenthal, V. Ntziachristos, Looking at sound: optoacoustics with all-optical ultrasound detection, Light Sci. Appl. 7 (1) (2018) 53, https://doi.org/10.1038/s41377-018-0036-7.
[16] A. Dangi, S. Agrawal, S.-R. Kothapalli, Lithium niobate-based transparent ultrasound transducers for photoacoustic imaging, Opt. Lett. 44 (21) (2019) 5326–5329, https://doi.org/10.1364/OL.44.005326.
[17] H. Chen, S. Agrawal, A. Dangi, C. Wible, M. Osman, L. Abune, H. Jia, R. Rossi, Y. Wang, S.-R. Kothapalli, Optical-resolution photoacoustic microscopy using transparent ultrasound transducer, Sensors 19 (24) (2019) 5470. ⟨https://www.mdpi.com/1424-8220/19/24/5470⟩.
[18] R. Chen, Y. He, J. Shi, C. Yung, J. Hwang, L.V. Wang, Q. Zhou, Transparent high-frequency ultrasonic transducer for photoacoustic microscopy application, IEEE Trans. Ultrason. Ferroelectr. Freq. Control 67 (9) (2020) 1848–1853, https://doi.org/10.1109/TUFFC.2020.2985369.
[19] T. Liao, Y. Liu, J. Wu, L. Deng, Y. Deng, L. Zeng, X. Ji, Centimeter-scale wide-field-of-view laser-scanning photoacoustic microscopy for subcutaneous microvasculature in vivo, Biomed. Opt. Express 12 (5) (2021) 2996–3007, https://doi.org/10.1364/BOE.426366.
[20] S. Park, S. Kang, J.H. Chang, Optically transparent focused transducers for combined photoacoustic and ultrasound microscopy, J. Med. Bioeng. 40 (5) (2020) 707–718, https://doi.org/10.1007/s40846-020-00536-5.
[21] M. Chen, L. Jiang, C. Cook, Y. Zeng, T. Vu, R. Chen, G. Lu, W. Yang, U. Hoffmann, Q. Zhou, J. Yao, High-speed wide-field photoacoustic microscopy using a cylindrically focused transparent high-frequency ultrasound transducer, Photoacoustics 28 (2022), 100417, https://doi.org/10.1016/j.pacs.2022.100417.
[22] J. Park, B. Park, T.Y. Kim, S. Jung, W.J. Choi, J. Ahn, D.H. Yoon, J. Kim, S. Jeon, D. Lee, U. Yong, J. Jang, W.J. Kim, H.K. Kim, U. Jeong, H.H. Kim, C. Kim, Quadruple ultrasound, photoacoustic, optical coherence, and fluorescence fusion imaging with a transparent ultrasound transducer, Proc. Natl. Acad. Sci. USA 118 (11) (2021), e1920879118, https://doi.org/10.1073/pnas.1920879118.
[23] H. Chen, S. Mirg, M. Osman, S. Agrawal, J. Cai, R. Biskowitz, J. Minotto, S. R. Kothapalli, A high sensitivity transparent ultrasound transducer based on PMN-PT for ultrasound and photoacoustic imaging, IEEE Sens. Lett. 5 (11) (2021) 1–4, https://doi.org/10.1109/LSENS.2021.3122097.
[24] Y.-H. Liu, A. Kurnikov, W. Li, V. Kazakov, R. Ni, P. Subochev, D. Razansky, Sensitive ultrawideband transparent PVDF-ITO ultrasound detector for optoacoustic microscopy, Opt. Lett. 47 (16) (2022) 4163–4166, https://doi.org/10.1364/OL.462369.
[25] Y.H. Liu, L.X. Chen, C.Y. Li, F.S. Lin, H.Y. Su, C.T. Tsai, L.W. Wang, Y.H. Wang, C. H. Huang, Transparent flexible piezoelectric ultrasound transducer for photoacoustic imaging system, IEEE Sens. J. 22 (3) (2022) 2070–2077, https://doi.org/10.1109/JSEN.2021.3135872.
[26] C. Fang, H. Hu, J. Zou, A focused optically transparent PVDF transducer for photoacoustic microscopy, IEEE Sens. J. 20 (5) (2020) 2313–2319, https://doi.org/10.1109/JSEN.2019.2952971.
[27] C. Fang, J. Zou, Acoustic-resolution photoacoustic microscopy based on an optically transparent focused transducer with a high numerical aperture, Opt. Lett. 46 (13) (2021) 3280–3283, https://doi.org/10.1364/OL.423287.
[28] M.S. Osman, H. Chen, K. Creamer, J. Minotto, J. Liu, S. Mirg, J. Christian, X. Bai, S. Agrawal, S.R. Kothapalli, A novel matching layer design for improving the performance of transparent ultrasound transducers, IEEE Trans. Ultrason. Ferroelectr. Freq. Control 69 (9) (2022) 2672–2680, https://doi.org/10.1109/TUFFC.2022.3195998.
[29] J. Park, B. Park, U. Yong, J. Ahn, J.Y. Kim, H.H. Kim, J. Jang, C. Kim, Bi-modal near-infrared fluorescence and ultrasound imaging via a transparent ultrasound transducer for sentinel lymph node localization, Opt. Lett. 47 (2) (2022) 393–396, https://doi.org/10.1364/OL.446041.
[30] J. Park, B. Park, J. Ahn, D. Kim, J.Y. Kim, H.H. Kim, C. Kim, Opto-ultrasound biosensor for wearable and mobile devices: realization with a transparent ultrasound transducer, Biomed. Opt. Express 13 (9) (2022) 4684–4692, https://doi.org/10.1364/BOE.468969.
[31] D. Ren, C. Li, J. Shi, R. Chen, A review of high-frequency ultrasonic transducers for photoacoustic imaging applications, IEEE Trans. Ultrason. Ferroelectr. Freq. Control 69 (6) (2022) 1848–1858, https://doi.org/10.1109/TUFFC.2021.3138158.
[32] J.M. Cannata, T.A. Ritter, C. Wo-Hsing, R.H. Silverman, K.K. Shung, Design of efficient, broadband single-element (20–80 MHz) ultrasonic transducers for medical imaging applications, IEEE Trans. Ultrason. Ferroelectr. Freq. Control 50 (11) (2003) 1548–1557, https://doi.org/10.1109/TUFFC.2003.1251138.
[33] W. Xia, D. Piras, J.C.G. van Hespen, W. Steenbergen, S. Manohar, A new acoustic lens material for large area detectors in photoacoustic breast tomography, Photoacoustics 1 (2) (2013) 9–18, https://doi.org/10.1016/j.pacs.2013.05.001.
[34] G. Destgeer, J.H. Jung, J. Park, H. Ahmed, K. Park, R. Ahmad, H.J. Sung, Acoustic impedance-based manipulation of elastic microspheres using travelling surface acoustic waves, RSC Adv. 7 (36) (2017) 22524–22530.
[35] S. Thiagarajan, R.W. Martin, A. Proctor, I. Jayawadena, F. Silverstein, Dual layer matching (20 MHz) piezoelectric transducers with glass and parylene, IEEE Trans. Ultrason. Ferroelectr. Freq. Control 44 (5) (1997) 1172–1174, https://doi.org/10.1109/58.655643.
[36] C.-M. Wong, S.-F. Chan, W.C. Wu, C.-H. Suen, H.-M. Yau, D.Y. Wang, S. Li, J.Y. Dai, Tunable high acoustic impedance alumina epoxy composite matching for high frequency ultrasound transducer, Ultrasonics 116 (2021), 106506, https://doi.org/10.1016/j.ultras.2021.106506.
[37] K.H. Lam, H.-S. Hsu, Y. Li, C. Lee, A. Lin, Q. Zhou, E.S. Kim, K.K. Shung, Ultrahigh frequency lensless ultrasonic transducers for acoustic tweezers application, Biotechnol. Bioeng. 110 (3) (2013) 881–886, https://doi.org/10.1002/bit.24735.
[38] Z. Yong, Y. Junjie, V.W. Lihong, Tutorial on photoacoustic tomography, J. Biomed. Opt. 21 (6) (2016), 061007, https://doi.org/10.1117/1.JBO.21.6.061007.
[39] US-ANSI. ANSIZ136.1–2007 American National Standard for Safe Use of Lasers, Laser Institute of America, Orlando, (2007).
[40] H. Chen, S. Agrawal, M. Osman, J. Minotto, S. Mirg, J. Liu, A. Dangi, Q. Tran, T. Jackson, S.-R. Kothapalli, A transparent ultrasound array for real-time optical, ultrasound, and photoacoustic imaging, BME Front 2022 (2022), 9871098, https://doi.org/10.34133/2022/9871098.

Jiaming Zhang received his B.Sc. (Hons) degree in Biomedical Engineering from the Hong Kong Polytechnic University, and received M.Sc. degree in Biomedical Engineering from City University of Hong Kong. Starting from Oct 2020, he worked as a Research Assistant focusing on design and fabrication of ultrasound transducers. He is now pursuing his Doctoral degree at the Hong Kong Polytechnic University on ultrasound transducer applications.

Xing Long is a Ph.D. candidate in the Peking University/ Georgia Institute of Technology/ Emory University biomedical engineering joint Ph.D. program. She focuses on developing biomedical imaging device and processing imaging data from clinical studies, particularly in photoacoustic microscopy system and full-optical non-contact photoacoustic imaging system.

Guangjie Zhang received her Bachelor's degree from Beijing Forestry University and Ph.D. degree from Department of Biomedical Engineering, Peking University. Her work mainly focuses on system design and application of photoacoustic imaging technology.

Zhongtian Ma received the Bachelor of Engineering degree in Biomedical engineering from University of Electronic Science and Technology of China in 2018. He is currently working toward the Ph.D. degree in Biomedical engineering in the Department of Future Technology, Peking University. His research interests include miniature fluorescence microscope.

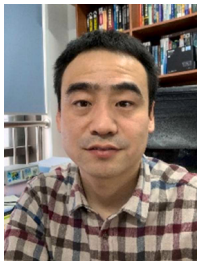

Wenzhao Li is an electronic engineer working in the Department of Biomedical Engineering, College of Future Technology, Peking University. His research focuses on analog electronic circuits, signal measurement, and embedded system design.

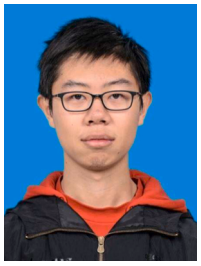

Yibing Wang is a Ph.D. student of Department of Biomedical Engineering in Peking University. He received his bachelor's degree in engineering from Peking University in 2021. Research interest: Photoacoustic Computed Tomography's image reconstruction and related medical image processing.

Fan Yang received the M.Sc. degree in Department of Electrical Engineering from the Hong Kong Polytechnic University (HKPolyU) in 2020. After worked as a Research Assistant from 2020 to 2021, he is now a Ph.D. candidate in Department of Electrical Engineering at HKPolyU. His research interests include the development of intelligent algorithms for state-of-charge estimation of batteries and signal processing in non-destructive evaluation.

Riqiang Lin received his M.Sc. and B.S. degree from Shenzhen University. He is currently pursuing his Doctoral degree at the Hong Kong Polytechnic University and focuses on the research work of photoacoustic endoscopy imaging and ultrasound transducer technology. He has developed a series of novel photoacoustic systems including optical resolution and acoustic resolution photoacoustic microscopy, and full field-of-view photoacoustic endoscopy.

Changhui Li is an associate professor in the department of Biomedical Engineering of Peking University. He received his B.Sc. degree in 1997 from Peking University and Ph.D. degree in 2006 from Texas A&M University. Prior to joining Peking University, he worked at Washington University, St. Louis as a post doctor from 2006 to 2010. His research focuses on developing novel biomedical imaging methods, including photoacoustic imaging and fluorescence imaging.

Kwok-ho (Koko) LAM is a Reader (Ultrasonics) in James Watt School of Engineering at the University of Glasgow and an Adjunct Professor in Department of Electrical Engineering at the Hong Kong Polytechnic University (HKPolyU). He received the M.Phil. and Ph.D. degrees in Applied Physics from HKPolyU. After working as a Postdoctoral Fellow at HKPolyU, he became a Research Associate at the NIH Resource Center on Medical Ultrasonic Transducer Technology in the Department of Biomedical Engineering of University of Southern California. He started his academic career as an Assistant Professor and later an Associate Professor and Associate Head of Department in Electrical Engineering at HKPolyU. His research focuses on materials for energy conversion and storage, ultrasound transducer technology for biomedical and non-destructive evaluation applications, and multimodal imaging technology. He has achieved 220 + publications, including 7 granted patents for 6 inventions, 190 + SCI journal papers, and 20 international conference papers. He was a recipient of the Early Career Award presented by Research Grants Council of Hong Kong in 2014. He is a Senior Member of the IEEE Society and an Exco member of Ultrasound Transducers and Materials Society, China Association of Medical Equipment - Medical Ultrasound Equipment Society.